Testing the efficacy of atmospheric boundary layer height detection algorithms using uncrewed aircraft system data from MOSAiC

Gina Jozef[1,2,3], John Cassano[1,2,3], Sandro Dahlke[4], Gijs de Boer[2,5,6]

[1]Dept. of Atmospheric and Oceanic Sciences, University of Colorado Boulder, Boulder, CO, USA
[2]Cooperative Institute for Research in Environmental Sciences, University of Colorado Boulder, Boulder, CO, USA
[3]National Snow and Ice Data Center, University of Colorado Boulder, Boulder, CO, USA
[4]Alfred Wegener Institute Helmholtz Centre for Polar and Marine Research, Potsdam, Germany
[5]NOAA Physical Sciences Laboratory, Boulder, CO, USA
[6]Integrated Remote and In Situ Sensing, University of Colorado Boulder, Boulder, CO, USA

Correspondence to: Gina Jozef (gina.jozef@colorado.edu)

Abstract. During the Multidisciplinary drifting Observatory for the Study of Arctic Climate (MOSAiC) expedition, meteorological conditions over the lowest 1 km of the atmosphere were sampled with the DataHawk2 (DH2) fixed wing uncrewed aircraft system (UAS). Of particular interest is the atmospheric boundary layer (ABL) height, as ABL structure can be closely coupled to cloud properties, surface fluxes, and the atmospheric radiation budget. The high temporal resolution of the UAS observations allows us to subjectively identify ABL height for 65 out of the total 89 flights conducted over the central Arctic Ocean between 23 March and 26 July 2020 by visually analyzing profiles of virtual potential temperature, humidity, and bulk Richardson number. Comparing this subjective ABL height with the ABL heights identified by various previously published objective methods allows us to determine which objective methods are most successful at accurately identifying ABL height in the central Arctic environment. The objective methods we use are the Liu-Liang, Heffter, virtual potential temperature gradient maximum, and bulk Richardson number methods. In the process of testing these objective methods on the DH2 data, numerical thresholds were adapted to work best for the UAS-based sampling. To determine if conclusions are robust across different measurement platforms, the subjective and objective ABL height determination processes were repeated using the radiosonde profile closest in time to each DH2 flight. For both the DH2 and radiosonde data, it is determined that the bulk Richardson number method is the most successful at identifying ABL height, while the Liu-Liang method is least successful.

1 Introduction

The transfer of energy between the Earth's surface and the overlying atmosphere, particularly at high latitudes, remains an area of substantial uncertainty in our understanding of the global climate system (de Boer et al., 2012; Tjernström et al., 2012; Karlsson and Svensson, 2013). The consequences of this uncertainty are significant, with global climate model projections of present-day sea ice demonstrated to fall short of simulating the observed rate of change (Stroeve et al., 2007; Stroeve et al., 2012). The thermodynamic structure of the lower atmosphere plays a central role in regulating cloud lifecycle and radiative transfer, and their influence on atmospheric energy transport (Tjernström et al., 2004; Karlsson and Svensson, 2013; Brooks et al., 2017). Significant insight can be gained by measurements

collected over the central Arctic Ocean ice pack, focused on the structure of the lower atmosphere, its spatial and temporal variability, the intensity of turbulent energy fluxes, and its connection to surface features. To provide such measurements, uncrewed aircraft were deployed in the lower atmosphere during legs 3 (March through May 2020) and 4 (June through August 2020) of MOSAiC (Multidisciplinary drifting Observatory for the Study of Arctic Climate; Shupe et al. 2020), a year-long expedition that took place from October 2019 to September 2020 in which the icebreaker *RV Polarstern* (Alfred-Wegener-Institut Helmholtz-Zentrum für Polar- und Meeresforschung, 2017) was frozen into the central Arctic ocean sea ice pack and allowed to passively drift across the central Arctic for an entire year (Fig. 1). Additional information on measurements taken of the atmosphere and sea ice during MOSAiC can be found at Shupe et al. (submitted) and Nicolaus et al. (submitted) respectively.

One component of the structure of the lower Arctic atmosphere is the atmospheric boundary layer (ABL) height. The ABL is the turbulent lowest part of the atmosphere that is directly influenced by the earth's surface (Stull, 1988; Marsik et al., 1995). In the central Arctic, the ABL is mostly impacted by interactions between the atmosphere and sea ice surface features, including the generation of turbulence through surface energy fluxes emitted from open water regions such as leads (Lüpkes et al., 2008), the horizontal advection of airmasses from lower latitudes (Brooks et al., 2017), radiative mixing forced by cloud cover (Tjernström et al., 2004), or mechanical generation of turbulence by sea ice features (Andreas et al., 2010) or oceanic waves (Jenkins et al., 2012). Solar heating of the earth's surface and the subsequent formation of buoyant thermals, which is a dominant forcing of the ABL in most parts of the planet (Marsik et al., 1995), does not often play a role in the central Arctic due to the relatively reflective surfaces found there. To understand the influence of the surface on other atmospheric features such as clouds and their influence on radiative transfer in the lower atmosphere, low level jets, and temperature inversions, it is important to identify the ABL height.

The depth of the ABL has been previously defined using a variety of approaches that involve visualizing the profiles of different variables. Table 1 lists the variables that have previously been used to identify ABL height, as well as the associated literature that references use of that variable. Each of these variable profiles typically exhibits a distinct change in structure at the top of the ABL, which is why they are used to identify ABL height.

Table 1 goes here

Of these methods, some of the most widely used ones, and the ones applied in the current analysis of a central Arctic dataset to determine ABL height are the ones that involve analysis of virtual potential temperature (θ_v), vertical gradient of virtual potential temperature ($d\theta_v/dz$), humidity, bulk Richardson number (Ri_b), and wind speed profiles. The current focus is on these variables because the physical basis for each one as an indication of ABL height is relevant for the Arctic atmosphere. Specifically, θ_v helps identify the entrainment zone above the ABL, humidity begins to either decrease or increase more above the ABL (Dai et al., 2014), Ri_b helps identify where turbulence (caused by buoyancy in a convective ABL (Stull, 1988) and by strong wind shear or surface roughness in a stable or

neutral ABL (Grachev et al., 2005)) ceases above the ABL, and wind speed helps identify the top of the ABL when it is capped by a low-level jet (Stull, 1988).

High resolution data collected by the DataHawk2 uncrewed aircraft system (UAS) allows for determination of ABL
80 heights with high accuracy through visual analysis of profiles of θ_v, humidity, and Ri_b. However, visually determining ABL height case-by-case is time consuming for processing a large dataset. Therefore, the UAS-derived dataset is leveraged to compare subjectively determined ABL heights with those identified through previously published objective and automated methods. This evaluation is completed to identify objective methods that can accurately diagnose ABL height across a larger dataset of central Arctic atmospheric conditions.

85

To subjectively identify the ABL height of each atmospheric profile from DH2 data, the stability regime of the ABL (stable, neutral, or convective) is categorized and ABL heights are visually identified through combined evaluation of θ_v, humidity (both relative humidity (RH) and mixing ratio), and Ri_b profiles. Objective analyses of ABL heights are derived through the application of previously published methods, including those in Liu and Liang (2010), Heffter
90 (1980), Dai et al. (2014), and Sivaraman et al. (2013), adapted to best suit the DH2 profiles examined. Then, statistical comparisons of the objective ABL heights and the subjective values are conducted to evaluate how well each method identifies the correct ABL height. Next, the objective methods are applied in their adapted form to radiosonde profiles nearest in time to each DH2 flight to determine if these methods are robust across different measurement platforms for central Arctic conditions. Finally, discussion is included on the features that do or do not lend themselves to
95 accurate identification of the ABL height by the objective methods, and findings are summarized to support future studies seeking to identify ABL height quickly, objectively, and accurately across large atmospheric datasets collected in the central Arctic.

2 Data and methods
100 ### 2.1 The DataHawk2
Data presented in this paper were obtained between 23 March and 26 July 2020 using the University of Colorado DataHawk2 (DH2) UAS (de Boer et al. submitted). Flights were conducted from the sea ice alongside the *Polarstern*, known as the MOSAiC floe, ranging in location from 86.2° N, 15.8° E on 23 March, to 79.8° N, 1.9° W on 26 July 2020 (Fig. 1). Throughout this time period, the MOSAiC floe evolved from snow-covered rigid ice situated in the
105 high Arctic to being covered with melt ponds and leads close to the sea ice edge. The surface atmospheric temperatures also transitioned from nearly -35° C at the beginning of leg 3 to hovering around 0° C throughout the entirety of leg 4.

Figure 1 goes here

110

The DH2 (Hamilton et al., in progress) is a fixed wing, battery powered UAS (1.1 m wingspan, 1.8 kg weight, 40-minute endurance) carrying various meteorological sensors. Instrumentation includes a fine wire array providing high

frequency (800 Hz) information on temperature and air speed, multiple sensors for temperature and relative humidity (Vaisala RSS-421 measuring at 5 Hz and SHT-85 measuring at 100 Hz), and up- and downward looking thermopile

115 sensors to provide infrared brightness temperatures of the sky and surface. Air pressure is measured at 5 Hz by the Vaisala RSS-421 sensor. Measurements of attitude, airspeed, ground speed, and altitude support the derivation of high-frequency (10 Hz) 3D wind estimates. Combined, these sensors provide a comprehensive picture of atmospheric thermodynamic and kinematic state along with some context on the surface and sky condition under which these measurements were obtained. Table 2 lists the resolution, repeatability (standard deviation of difference between two

120 successive repeated calibrations), and response time for the Vaisala RSS-421 sensor. Uncertainty in the wind speed estimation is not provided, as determining this is still in progress.

Table 2 goes here

125 Measurements collected by the DH2 are logged at different frequencies, requiring the implementation of a time alignment process to assure that the time index for each datapoint of each variable is consistent with all other measurements. Additionally, the wind measurements have been filtered to remove the impact of the angle and ground speed of the aircraft to provide estimates of the true wind speed (de Boer et al., in progress). Data collected by the DH2 during MOSAiC are available for public download through the NSF Arctic Data Center at *insert DOI when

130 available* (Jozef et al., 2021).

During MOSAiC, DH2 flights were conducted whenever flight weather criteria were met and when the team was able to access the ice alongside the *Polarstern*. The weather criteria include wind speeds with a sustained average below 10 m s^{-1}, and gusts below 14 m s^{-1}, as well as sufficient visibility to maintain visual contact with the aircraft at all

135 times during flight. In addition, the DH2 flights required coordination with other MOSAiC activities, especially those impacting air space over the MOSAiC floe, including manned helicopter flights and other UAS and tethersonde operations. Since the DH2 flights were limited to days in which these weather and airspace criteria were met, the profiles sampled during the campaign only represent those that occurred under a subset of all conditions observed during legs 3 and 4 of MOSAiC.

140

The most common flight pattern conducted with the DH2, and the flight pattern from which data for this analysis were acquired, was a profiling flight in which the plane flew a spiral ascent and descent pattern, with a radius of 75-100 m between the surface and 1 km altitude (or cloud base, if lower than 1 km), with the aircraft ascending and descending at a rate of 2 m s^{-1} and flying at an airspeed of 14-18 m s^{-1}. Each profiling flight lasted an average of 30-minutes, with

145 some shorter flights when the air temperature was at its coldest (~-35 °C) near the beginning of leg 3, and some longer flights when the air temperature was much warmer (~0 °C) during leg 4. Throughout our measurement period, 89 flights were conducted with the DH2. In the present study, 65 of these flights are found to have clearly identifiable ABL heights within the altitude range sampled. The remaining flights sampled only the lowest portion of the

150   atmosphere due to cloud cover or other environmental conditions and therefore did not observe the full depth of the ABL.

For each of these 65 DH2 flights, the ABL height is visually determined from the θ_v, humidity, and Ri_b profiles; the former two of which have been created by averaging each variable in 1 m bins throughout the flight, excluding the first 5 seconds of flight, as the initial measurements after takeoff may be faulty due to hysteresis associated with the

155   sensor sitting still at the surface before launch. Additionally, the ABL heights are objectively identified using the four published methods (Liu-Liang, Heffter, virtual potential temperature gradient maximum method, and the bulk Richardson number method). For the remainder of the manuscript, ABL heights determined from visual identification are referred to as the "subjective" ABL heights and the ABL heights determined by the published methods are referred to as the "objective" ABL heights. Some of the methods for both subjectively and objectively identifying ABL height

160   differ depending on the stability regime, so the sampled regime is first identified for each DH2 flight. Once the regime is defined, we apply the appropriate criteria below to subjectively identify the ABL height for each case and compare this to the ABL height identified by each of the published objective methods.

Lastly, profiles of potential temperature, humidity, and wind speed from the balloon-borne radiosondes that were

165   launched at least 4 times per day from the deck of the *Polarstern* (Maturilli et al., 2021) are leveraged to determine if the objective methods used to identify ABL height from the UAS data are robust across platforms. To do this, radiosonde profiles with launch times closest to DH2 flight times are used, repeating the same processes for subjective and objective ABL height identification and comparison.

170   **2.2 Determining stability regime**

The three possible stability regimes considered include a convective boundary layer (CBL), stable boundary layer (SBL), and neutral boundary layer (NBL; Liu and Liang, 2010). A CBL forms when convective thermals create positive buoyancy (Liu and Liang, 2010) and an air parcel at the surface rises adiabatically until becoming neutrally buoyant. In a CBL, θ_v near the surface is greater than that of the overlying ABL (Stull, 1988). A SBL forms when

175   there is a deficit of radiation at the surface, or when warmer air is advected over a cooler surface. In a SBL, θ_v increases with altitude, and can range from being nearly well-mixed with moderate turbulence to nearly laminar (Stull, 1988), though some amount of turbulence is always present. A NBL occurs when there are near-neutral conditions in the ABL (Sivaraman et al., 2013), meaning requirements are lacking for either a CBL or SBL, air at the surface is neutrally buoyant, and θ_v at the surface is approximately the same value as that of the overlying remainder of the ABL (Stull,

180   1988).

Stability regimes are identified by comparing θ_v (calculated using RSS-421 temperature, pressure, and RH) between the lowest altitude sampled by the DH2 (*i*; typically ~5m) and 40 m above using equations 1-3 below adapted from Liu and Liang (2010).

185

$$\theta_{v_{i+40m}} - \theta_{v_i} < -\delta_s = \text{CBL} \qquad (1)$$

$$\theta_{v_{i+40m}} - \theta_{v_i} > +\delta_s = \text{SBL} \qquad (2)$$

$$-\delta_s \leq \theta_{v_{i+40m}} - \theta_{v_i} \leq +\delta_s = \text{NBL} \qquad (3)$$

190   In these equations, δ_s is a stability threshold that represents the minimum θ_v increase/decrease with altitude near the surface necessary for the ABL to qualify as a SBL/CBL. If this minimum is not reached in either direction, the ABL is identified as a NBL (Liu and Liang, 2010). In an idealized case, δ_s would be zero. However, in practice it must be specified as a small positive number, and this number depends on the surface characteristics. For profiles over ocean/ice, this number has been defined to be 0.2 K (Liu and Liang, 2010).

195

    While Liu and Liang (2010) compare θ_v between pressure levels that equate to approximately 40 and 160 m in the conditions we sampled, this range was found to be inadequate for differentiating between a SBL, NBL or CBL. In the current study, ABL tops were observed to range in height between 38-287 m, with an average of 104 m. This means that the 40 – 160 m altitude range used by Liu and Liang (2010) would include all of the boundary layer and a portion

200   of the overlaying free atmosphere for most cases. This would result in the incorrect identification of most ABLs as SBLs, since the overlaying free atmosphere will always have a greater θ_v than that of the ABL. In general, considering the θ_v change below ~45 m more accurately reflects the stability regime of the Arctic ABL, since the ABL is often much shallower than that over land or at midlatitudes (Esau and Sorokina, 2010).

205   Once the stability regime (CBL, NBL, or SBL) is identified, criteria based on the θ_v, humidity, and Ri_b profiles are applied to subjectively determine the boundary layer height. For the current dataset, 31 SBL cases, 32 NBL cases, and 2 CBL cases were identified. This is in agreement with Brooks et al. (2017), which states that the ABL over sea ice in the summer is typically near-neutral or weakly stable, and our data suggests this is also true in the late winter to spring season.

210

2.3 Subjective identification of atmospheric boundary layer height

    To subjectively identify ABL height, the θ_v profile is first analyzed, as the θ_v profile changes structure above the ABL (Stull ,1988). For a CBL and NBL, above the ABL, θ_v changes from decreasing or constant with height, to increasing with height, marking the entrainment zone (Stull, 1988). The structure of a SBL, however, can vary a lot more (Mayer

215   et al., 2012; Steeneveld et al., 2007; Zilitinkevich and Baklanov, 2002). In an ideal SBL case, the θ_v inversion is at its strongest near the surface and transitions to the free atmosphere (nearly constant or gradually increasing θ_v with altitude) above the SBL, with no entrainment zone (Stull, 1988). The ABL height is then identified as the altitude of the shift from the surface based θ_v inversion to the free atmosphere (Stull, 1988). In reality, the structure of a SBL is often not that simple, and the height of a SBL can be difficult to identify based on θ_v alone (Stull, 1988; Zhang et al.,

220   2014). SBLs in our dataset often included a weaker surface based θ_v inversion capped by a layer of enhanced stability (stronger θ_v inversion), reminiscent of an entrainment zone. ABLs with this structure form as the near-surface atmosphere fluctuates between weakly stable and near-neutral (Brooks et al., 2017). In more difficult cases such as

these, the top of the SBL can be better determined by supplementing the θ_v profile with the RH and mixing ratio profiles, which usually have an obvious transition at the top of the ABL (Dai et al., 2014), as well as the Ri_b profile (Zhang et al., 2014).

Bulk Richardson number is the ratio between buoyantly (from thermals) and mechanically (from wind shear) produced turbulence (Sivaraman et al., 2013). The buoyancy term can also indicate that stability is suppressing turbulence. Therefore, Ri_b can help to identify the top of the ABL under the assumption that turbulence ceases above of the ABL (Stull, 1988), and thus, Ri_b will exceed a critical value (typically 0.25; Stull, 1988) at the top of the ABL (Seibert et al., 2000). Ri_b is calculated at altitude, z, using the following equation from Stull (1988):

$$Ri_b(z) = \frac{\left(\frac{g}{\theta_v}\right) \Delta \theta_v \, \Delta z}{\Delta u^2 + \Delta v^2} \qquad (4)$$

where g is acceleration due to gravity, $\overline{\theta_v}$ is mean virtual potential temperature over the altitude bin being considered, z is altitude, u is zonal wind, v is meridional wind, and Δ represents the difference over the altitude bin used to calculate Ri_b throughout the profile. The only way that Ri_b can be negative is if the value for $\Delta\theta_v$ is negative, indicating a convective atmosphere with buoyancy-driven generation of the turbulence.

Ri_b values below the critical threshold (often taken as ~0.25) indicate a turbulent atmosphere, while values above this threshold indicate that an already laminar layer will not become turbulent, as static stability is strong enough to suppress mechanically generated turbulence. While the critical value of 0.25 is not always the exact number that corresponds to the transition between turbulent and laminar conditions (different studies have used critical Richardson numbers ranging from as low as 0.15 to as high as 7.2 in coarse resolution models; Dai et al., 2014), low Ri_b is generally expected in the ABL, and high Ri_b is expected above the ABL. By examining Ri_b profiles for our DH2 flights, this transition from values near or below 0.25 to well above 0.25 can be identified to mark the top of the ABL. Ri_b profiles are created by calculating Ri_b over 30 m bins, at 5 m resolution.

2.3.1 Subjective atmospheric boundary layer height for a CBL

To determine the ABL height of a CBL, we identify the bottom of the entrainment zone. From the surface, the θ_v of a CBL decreases with altitude (Stull, 1988). Therefore, to identify the height of a CBL, we identify the altitude at which the potential temperature has returned to its surface value and then increases with altitude. This will not be the first altitude at which the θ_v increases with altitude. Rather, this will be the bottom of a layer of enhanced stability (stronger θ_v inversion) above. For one of the CBL cases we sampled, this altitude is also accompanied by a large increase in Ri_b above this altitude, and a shift from increasing to decreasing RH with height (Fig. 2a).

2.3.2 Subjective atmospheric boundary layer height for a NBL

To determine the height of a NBL, the θ_v profile is first referenced, looking for the altitude at which the θ_v shifts from being approximately constant with altitude to increasing with altitude. This marks the shift from the mixed layer, or

260   ABL, to the entrainment zone above (Stull, 1988). Figure 2b shows an example of a profile with a single shift in θ_v
slope around 110 m altitude. If there is more than one shift in slope of θ_v within the same θ_v inversion, a kink (abrupt
slope shift) in the RH and/or the mixing ratio profiles can be used to identify which θ_v slope shift indicates the top of
the ABL. Typically, this kink indicates a shift from RH that is increasing or constant with altitude, to decreasing with
altitude, however a few cases feature a humidity inversion (ex: Fig. 2c), meaning the kink indicates a shift from RH
265   increasing with altitude to RH increasing even more with altitude. This spot on the profile is usually accompanied by
a large increase in Ri_b above this altitude. Figure 2c shows an example of a profile with multiple shifts in θ_v slope,
where the shift associated with a kink in the RH and mixing ratio profiles around 100 m is selected.

The third possibility is a rarer NBL case in which there is no clear elevated θ_v inversion layer above the layer of
270   constant θ_v with altitude. Rather, θ_v slowly shifts to a steady increase with altitude throughout the profile. In this case,
there is no clear indication from the θ_v profile as to where the top of the ABL is, so the determination is made entirely
on the humidity and Ri_b profiles. Once a shift is identified where Ri_b goes from consistently being very small to very
large that coincides with a kink in the humidity profiles, the θ_v profile is reanalyzed for a visually detectable (as slight
as it may be) shift in slope near the altitude indicated by the Ri_b and humidity profiles, and we identify this as the ABL
275   top (Fig. 2d).

2.3.3 Subjective atmospheric boundary layer height for a SBL
Determining the height of a SBL is more difficult, since the low-level θ_v inversion extends to the surface. However,
the DH2 data from MOSAiC include very few cases in which the surface based θ_v inversions are at their strongest
280   right from the surface. Instead, the static stability strengthens some distance above the surface in almost every stable
case, likely because of surface-drag induced turbulence close to the surface. Additionally, many SBL cases are close
to meeting the criteria to be a NBL. Therefore, similar criteria to those used to determine NBL height are applied for
evaluating SBL height. This includes identification of the altitude at which stability is enhanced and θ_v increases more
with altitude than it did in the layer below. This altitude usually corresponds to a kink in the humidity profiles and a
285   shift in the Ri_b profile from near 0.25, to well above 0.25. Figure 2e shows a representative example where this
approach is applied.

For cases that do not include an obvious stability transition in the θ_v profile, more attention is given to the humidity
and/or Ri_b profiles. In these cases, a slope shift in the humidity profiles is identified first, after which the θ_v profile is
290   evaluated for any slight variability to identify the top of the ABL (Fig. 2f). The humidity profiles are more helpful
than the Ri_b profile in many SBL cases, as the Ri_b profile usually does not include any clear shift at the top of a SBL.
However, there are some limited cases in which Ri_b shifts from below to above critical at the top of the SBL, and in
those cases this information is helpful in determining the correct height for the top of ABL.

295   **Figure 2 goes here**

2.4 Objective identification of atmospheric boundary layer height

After subjectively identifying the ABL height for each profile using visual techniques, several published methods for objectively determining ABL height are also applied and evaluated. Through this analysis, the usefulness of each objective method for evaluating ABL height in the central Arctic is assessed. The objective methods that are implemented include the Liu and Liang (2010), the Heffter (1980), the virtual potential temperature gradient maximum (TGRDM; Dai et al., 2014), and the bulk Richardson number (Ri_b) methods (Sivaraman et al., 2013).

Each of these methods relies on profiles of either $d\theta_v/dz$ or Ri_b, some in combination with the θ_v and/or wind speed profiles. As for the Ri_b profiles, $d\theta_v/dz$ profiles are created by calculating $d\theta_v/dz$ over 30 m bins, at 5 m resolution.

2.4.1 Liu-Liang method

The Liu-Liang method is applied in slightly different ways depending on whether the profile includes a CBL, SBL, or NBL. Each off these different implementations are described in the following subsections.

2.4.1.1 Liu- Liang method for a CBL

For a CBL, the ABL height is determined as the height at which an air parcel rising adiabatically from the surface first becomes neutrally buoyant (Stull, 1988). To implement the Liu-Liang method for this type of profile, the lowest altitude, j, in which the following criterion is met is identified:

$$\theta_{v_j} - \theta_{v_i} \geq \delta_u \tag{5}$$

where i is the lowest altitude sampled by the DH2 and δ_u is the θ_v difference that represents the minimum strength of the θ_v inversion necessary to indicate the transition from the ABL to the entrainment zone above. δ_u is defined to be 0.1 K for atmosphere above an ocean/ice surface (Liu and Liang, 2010). In essence, this equation seeks to find the lowest altitude at which θ_v exceeds its surface value by 0.1K.

Next, the lowest altitude, k, above j, where the virtual potential temperature gradient ($\dot{\theta}_k$) is greater than $\dot{\theta}_r$ according to equation 6 below from Liu and Liang (2010) is identified:

$$\dot{\theta}_k \equiv \frac{d\theta_v}{dz}(k) \geq \dot{\theta}_r \tag{6}$$

where $\dot{\theta}_r$ is the minimum strength for the overlying θ_v inversion necessary to identify the top of the ABL, and is specified to be 0.05 K/100 m over ocean/ice by Liu and Liang (2010). The altitude determined by this method is then considered the ABL height for a CBL. The Liu-Liang method applied to a CBL case is shown in Fig. 3a.

2.4.1.2 Liu-Liang method for a NBL

The Liu-Liang method for determining the height of a NBL states that the height of the NBL is the altitude at which $d\theta_v/dz$ first exceeds 0.05 K/100 m. However, this threshold was found to be inappropriate for the current dataset, so instead a threshold of 2.5 K/100 m is applied. The first altitude at which $d\theta_v/dz$ exceeds 2.5 K/100 m is identified and defined to be the ABL height. Figure 3b shows an example of this adapted Liu-Liang method applied to a NBL case using the threshold of 2.5 K/100m, as well as what the Liu-Liang ABL height would have been using the original threshold of 0.05 K/100m, with a dotted line.

2.4.1.3 Liu-Liang method for a SBL

There is no recognized equation to determine SBL top height accurately without observations supporting the derivation of turbulent kinetic energy profiles (Stull, 1988; Siebert et al., 2000). However, as a SBL can either be minimally turbulent due to lack of buoyancy below the ABL or more turbulent due to the presence of wind shear (Stull, 1988), Liu and Liang (2010) search for potential ABL heights associated with each scenario. Thus, for a SBL, ABL height is defined as either the top of the bulk stable (θ_v inversion) layer starting from the ground, or the height of the low-level jet (LLJ) maximum if present, whichever is lower (Liu and Liang, 2010).

To find the height of a SBL defined by a lack of buoyancy, a local minimum in $d\theta_v/dz$ is identified (Liu and Liang, 2010). To be identified as the ABL height, the altitude, k, of this local $d\theta_v/dz$ minimum must meet one of the following two conditions outlined in Liu and Liang (2010):

$$\dot{\theta}_k - \dot{\theta}_{k-40m} < -\dot{\delta} \tag{7}$$
or
$$[\dot{\theta}_{k+40m} < \dot{\theta}_r \text{ and } \dot{\theta}_{k+80m} < \dot{\theta}_r] \tag{8}$$

where $\dot{\theta}_k = d\theta_v/dz$ at altitude k, $\dot{\delta} = 4$ K/100 m, and $\dot{\theta}_r$ is 0.05 K/100 m over ocean/ice (Liu and Liang, 2010). Under the first condition, the ABL top is positioned at the altitude where there is sufficient diminishment of the surface θ_v inversion. If no point in the profile meets this first criterion, the second criterion is tested, which attempts to identify the first local minimum at altitude, k, in which $d\theta_v/dz$ both 40 and 80 m above k are less than $\dot{\theta}_r$. This indicates that the θ_v inversion has consistently diminished above altitude, k.

Lastly, LLJ presence is identified by searching for wind speeds reaching a maximum that is at least 2 m s⁻¹ stronger than the layers above and below (Stull, 1988; Liu and Liang, 2010). If the altitude of the LLJ is below the ABL height determined by one of the above two conditions, the ABL height is adjusted to the LLJ height (example shown in Fig. 3d), If the LLJ is above the previously determined ABL height, then the altitude given by the above conditions is preserved as the ABL height (example shown in Fig. 3c; Liu and Liang, 2010).

Figure 3 goes here

2.4.2 Heffter method

The Heffter method uses θ_v difference across a θ_v inversion as an indication of ABL height (Sivaraman et al., 2013). For a CBL or NBL, this method is meant to determine the altitude of the elevated θ_v inversion marking the entrainment zone between the mixed layer and free atmosphere (Pesenson, 2003). For a SBL, this method determines where the change in strength of the surface θ_v inversion marks the transition from the ABL to residual layer or free atmosphere above (Stull, 1988).

The Heffter method identifies the top of the ABL by identifying where $d\theta_v/dz$ is greater than 0.5 K/100 m throughout the θ_v inversion, and the θ_v difference across the θ_v inversion ($d\theta_v$) is at least 2 K (Heffter, 1980; Pesenson, 2003; Sivaraman et al., 2013). This is summarized by equations 9 and 10 below from Heffter (1980):

$$\frac{d\theta_v}{dz} > 0.5 \; K/100m \tag{9}$$

and

$$\theta_{v_t} - \theta_{v_b} > 2 \; K \tag{10}$$

where θ_{v_t} is θ_v at the top of the θ_v inversion and θ_{v_b} is θ_v at the bottom of the θ_v inversion (Heffter, 1980; Pesenson, 2003).

To apply this method, the bottom and top of a θ_v inversion are first identified by determining where $d\theta_v/dz$ first goes above 0.5 K/100 m (for the bottom), and then again goes below 0.5 K/100 m at an altitude above the θ_v inversion base (for the top) (Sivaraman et al., 2013). For some SBL cases, the θ_v inversion extends to the surface, so $d\theta_v/dz$ at the lowest altitude measured by the DH2 is already greater than 0.5 K/100 m. In these cases, the bottom of the $d\theta_v/dz$ profile is identified as the θ_v inversion bottom. For other cases, the θ_v inversion starts near the top of the profile, but $d\theta_v/dz$ does not go below 0.5 K/100 m again within the altitude range sampled. In these cases, θ_v at the inversion base and at the top of the profile are compared to see if the second criterion is met.

Once all θ_v inversions are identified, the lowest layer in which θ_v at the top of the inversion is at least 2 K greater than at the bottom of the inversion is chosen (Sivaraman et al., 2013). Within this θ_v inversion, the altitude at which θ_v first becomes more than 2 K greater than θ_v at the bottom of the θ_v inversion is labelled as the ABL height (Marsik et al., 1995; Delle Monache et al., 2004; Snyder and Strawbridge, 2004; Sivaraman et al., 2013).

This method can be applied regardless of stability regime to find ABL height (Sivaraman et al., 2013). Figure 4 below shows an example of the Heffter method applied to a case for each stability regime. For the NBL and SBL examples shown, the Heffter method identifies ABL heights close to the subjective values. For the CBL case, there is no θ_v inversion layer in the altitude range sampled across which the θ_v difference is more than 2K, so the Heffter method fails to find an ABL height.

375

380

385

390

395

400

405

Figure 4 goes here

2.4.3 Virtual potential temperature gradient maximum (TGRDM) method

The final $d\theta_v/dz$-based method used to find the ABL height is the virtual potential temperature gradient maximum (TGRDM) method (Dai et al., 2014). Since the ABL is typically capped by a well-defined θ_v inversion layer (Stull, 1988), even in a weakly stable case, we expect to see a peak in the $d\theta_v/dz$ profile at this point. By finding the maximum in the $d\theta_v/dz$ profile, the altitude at which the θ_v inversion is at its strongest and weakens above is identified.

To apply this method, peaks in the $d\theta_v/dz$ profile where $d\theta_v/dz$ is at least 1.75 K/100 m greater than a minimum $d\theta_v/dz$ above are identified. This helps to identify robust peaks, eliminating false positives resulting from small variability in the profile. It is not required that $d\theta_v/dz$ at the peak be 1.75 K/100 m greater than a minimum $d\theta_v/dz$ below, otherwise an ABL height near the surface when there is a strong surface-based θ_v inversion will be missed. The ABL height is set to the altitude of this lowest peak. Figure 5 below shows an example of the TGRDM method applied to a case for each stability regime.

Figure 5 goes here

2.4.4 Bulk Richardson number method

Finally, a bulk Richardson number method for finding the ABL top is applied by determining the altitude at which Ri_b exceeds a critical value (Ri_{bc}). Previous literature suggests a wide range critical values with 0.25 (Stull, 1988) being the most widely accepted value, though a value of 0.5 is also often used (Sivaraman et al., 2013; Zhang et al., 2014). To determine a viable critical value for the DH2 data, a comparison between ABL heights determined from a range of critical values (we used $Ri_{bc} = 0.25, 0.5, 0.75, 1.0, 1.25,$ and 1.5) and the subjective ABL heights was conducted. In identifying the ABL height from these different Ri_{bc} values, the level above which Ri_b was consistently greater than the critical value was used to indicate where turbulence was no longer able to form in a laminar atmosphere. For this dataset, four consecutive datapoints (20 m) were required to be above the critical value. The altitude of the lowest of these four consecutive points is identified as the ABL height.

To determine which critical value consistently gives the best estimate of ABL height, the mean and maximum absolute difference between the ABL height given by each critical value and the subjective ABL height were calculated. Based on this evaluation, the critical value of 0.5 gives the lowest mean absolute difference, followed by 0.75. These two critical values also give the lowest maximum in the absolute difference. Therefore, further ABL heights presented using the Ri_b method are calculated with critical values of 0.5 and 0.75. Figure 6 below shows an example of the Ri_b method applied to a case for each stability regime.

Figure 6 goes here

445   Given that only DH2 cases in which the ABL top was clearly identifiable subjectively were used in the current
study, then if no altitude is found to satisfy the criteria for identifying ABL height using one the above objective
methods, then that objective method does not work to find the ABL height for that case.

2.5 Applying the objective methods to radiosonde profiles

450   As discussed above, some of the objective methods used in this study had to be modified from their original
descriptions to work with the Arctic UAS data. This is in part because previous implementations involved analysis of
radiosonde profiles and in mid-latitude locations. To determine if these modifications are robust across sensing
platforms, they are additionally applied to identify ABL height using radiosonde data from the MOSAiC expedition
(Maturilli et al., 2021). To do this, data from radiosondes launched within 3 hours of each DH2 flight were used to
455   repeat the processes outlined in section 2.3 for subjectively identifying ABL height using the θ_v, humidity, and Ri_b
profiles.

For each radiosonde profile, the θ_v (calculated from temperature, pressure, and humidity measurements) and wind
speed data were used to create the same profiles that were calculated using the DH2 data, and the same routines for
460   objectively identifying the ABL height from each method were applied (Liu-Liang, Heffter, TGRDM, and Ri_b). Before
applying the objective methods, data below 23 m altitude were removed, as the lowest part of the radiosonde profiles
were found to show inaccurately warm temperatures for several cases (Maturilli et al., 2021). Additionally, in some
cases, the radiosonde data showed anomalously warm measurements some distance above 23 m, which is assumed to
be the result of the balloon passing through the *Polarstern*'s exhaust plume. These measurements were adjusted by
465   interpolating the temperature between the closest good measurements above and below where the radiosonde was
presumably in the ship's plume. Since applying these adjustment means that radiosonde data near the surface are not
available, the stability regime for each profile is calculated by comparing θ_v between the lowest radiosonde
measurement and 30 m above, or the ABL height if lower, to the appropriate threshold value, δ_s, that is equal to (0.2
K/40 m) x the altitude range used. For example, if the 30 m altitude range is used, the value of δ_s is 0.15 K.
470

Figure 7 shows a comparison between the profiles used to objectively identify ABL height for a DH2 flight at 7:58
UTC and a radiosonde launched at 7:50 UTC on 14 April. This example shows that the subjective ABL heights
identified using the DH2 and radiosonde data are similar (differ by only 12 m), and that the objective methods reveal
a similar outcome when applied to the radiosonde data as they do for the DH2 data. This 5-panel plot showing objective
475   ABL height identification for all DH2 flights and associated radiosonde data can be found in Supplementary Figures
S1-S65.

Figure 7 goes here

480   While the radiosonde and DH2 profiles generally exhibit a similar structure due to the close time and space proximity
(the radiosondes were launched <600 m from the DH2 flights), the subjective ABL heights identified in those profiles

differ by 1-101 m. Generally, the closer in time that the DH2 and radiosonde were launched, the closer the subjective ABL height and objective ABL heights from the DH2 and radiosonde are to each other. Figure 8 shows the percent difference between DH2 and radiosonde subjective ABLs (top panel), as well as the percent difference between the

485 DH2 and radiosonde objective ABLs for each method (bottom panel) as a function of time difference in minutes between the DH2 and radiosonde launch. The best fit linear regression for each method shows that as time between the DH2 and radiosonde launch increases, the differences in ABL height increase as well. However, the increase in percent difference between subjective ABL height from the DH2 and radiosonde as time between the launches increases is not significant at the 5% significance level (probability value of 0.34). Therefore, we are confident that

490 the ABL height does not significantly change for DH2 and radiosonde launches up to 3.16 hours apart.

Figure 8 goes here

3. Results and discussion

495 **3.1 Efficacy of objective ABL height identification methods**

To determine how well the different objective methods worked, ABL heights identified by each objective method were compared to the subjective ABL heights. Figure 9 shows scatter plots comparing the objective to the subjective ABL height in each case, along with the associated best fit linear regression, coefficient of determination (R^2), slope value, and probability value (p-value) resulting from a paired two sample T-test. In some instances, there are two DH2

500 flights in closest time proximity to the same radiosonde launch, so in this case, the results from that radiosonde profile are plotted only once.

The R^2 value demonstrates a relationship between the objective and subjective ABL heights by explaining how much of the variation in the objective ABL height can be explained by the difference in subjective ABL height, with higher

505 R^2 values indicating a stronger relationship. Slope values are also included to help evaluate the level of correspondence between the subjective and objective ABL heights. Additionally, looking at the intercept combined with the slope value tells us whether the objective method tends to over- or underestimate ABL height. The line of best fit is included in dark blue (red) on Fig. 9a-e, which reflects the slope of the DH2 (radiosonde) datapoints written on each plot, and a line with slope of 1 and y-intercept of 0 is included in dashed black for reference. Lastly, the p-value tells us whether

510 the relationship between subjective and objective ABL height is significant at the 5% significance level (a p-value less than 0.05 indicates significance and vice versa).

Based on the DH2 data in these scatter plots, the method that gives the greatest R^2 value is the Ri_b method with critical value of 0. 5 (R^2 of 0.667, Fig. 9d), followed by the Ri_b method with critical value of 0.75 (R^2 of 0.537, Fig. 9e). These

515 are followed closely by the Heffter method (R^2 of 0.483, Fig. 9b). The TGRDM method has the fourth highest R^2 value (R^2 of 0.316, Fig. 9c). The only objective method with a very low R^2 value is the Liu-Liang method (R^2 of 0.0898, Fig. 9a). The slope values for all methods are within 0.3 of 1, the closest to 1 being the Ri_b method with critical value of 0.75 (slope of 1.02), followed TGRDM method (slope of 1.1) and Heffter method (slope of 1.17). These slope

values greater than 1 and positive intercept indicate that these methods generally overestimate ABL height when applied to the DH2 data. The Ri_b method with critical value of 0.5 and the Liu-Liang method, however, are more complex, as the slope values are both less than 1 (0.727 and 0.707 respectively), but the intercepts are both positive. This indicates that these methods overestimate ABL height for small ABL height, but underestimates it for large ABL height when applied to the DH2 data. Comparing the p-values for all relationships to the 5% significance level, then the relationship between subjective and objective ABL height is significant for every method (p-value is less than 0.05). These p-values follow the same order as the R^2 values, with the lowest p-value found for the Ri_b method with critical value of 0.5 (indicating the highest significance) and the highest p-value for the Liu-Liang method (indicating the lowest significance).

The radiosonde data gives a slightly different conclusion. Here, the method that gives the greatest R^2 value is the Heffter method (R^2 of 0.548, Fig. 9b), followed by the Ri_b method with critical value of 0.5 (R^2 of 0.392, Fig. 9d). The Ri_b method with critical value of 0.75 and the TGRDM method have lower R^2 values (0.182 and 0.209 and Fig. 9e and 9c, respectively). As was the case for the DH2 data, the only objective method with a very low R^2 number is the Liu-Liang method (R^2 of 0.0128, Fig. 9a), which is also echoed by a slope value far from 1, of 0.25. The slope values for the rest of the methods are not as close to 1 as they are for the DH2 data, but they are all within 0.5 of 1. The method with slope value closest to 1, and only method with slope greater than 1, is the Heffter method at 1.07, indicating that this method tends to overestimate ABL height when applied to the radiosonde data used in the current study. The rest of the methods have a slope of less than 1 and positive intercept, indicating that they tend to overestimate ABL height for small ABL height, but underestimate it for large ABL height when applied to the radiosonde data used in the current study. Lastly, the p-values follow the same order as the R^2 values, with the lowest p-value found for the Heffter method (indicating the highest significance) and the highest p-value for the Liu-Liang method (indicating the lowest significance). Unlike the DH2 results, for the radiosonde, the p-values for all relationships compared to the 5% significance level show that the relationship between subjective and objective ABL height is significant for every method except the Liu-Liang method, in which the p-value is greater than 0.05.

Lastly, Fig. 9f compares the subjective ABL height from the radiosondes to the subjective ABL height from the DH2. The line of best fit and associated R^2, slope value, and p-value are shown in purple, alongside a dashed black line of slope 1 and zero intercept for reference. The high R^2 value (0.779) indicates a strong correlation between the two subjective ABL heights, which demonstrates that the ABL height usually did not change much between the DH2 and radiosonde launches in each case. Interestingly, there is enhanced deviation from the line of best fit for lower ABL heights, and better agreement for higher ABL heights, indicating that the ABL height usually varied more between the DH2 and radiosonde launches for shallow ABLs. The very low p-value of 2.68e-22 demonstrates the high significance in the relationship between ABL heights from the DH2 and radiosondes.

Figure 9 goes here

In addition to evaluating general agreement between subjective and objective ABL heights for each method, additional analysis was completed to assess the frequency of objective ABL height determination within a certain percent difference from the subjective ABL height. To do this, an absolute percent difference between the objective and subjective ABL in each case and for each method was determined. These results are included in Fig. 10a for the DH2 profiles, and in Fig. 10b for the radiosonde profiles. For example, just over 30% of ABL heights predicted by the Liu-Liang method were within 10% of the subjective ABL height for the DH2 data.

Figure 10a shows that, for the DH2 profiles, the Ri_b method with critical value of 0.75 predicts the highest percent of cases to be within 10% of the subjective ABL height, followed by the Ri_b method with critical value of 0.5. Interestingly, the Liu-Liang method predicts the third highest percent of cases to be within 10% of the subjective ABL height. However, the Liu-Liang method falls behind other methods as the percent difference range is increased above 20%. Additionally, the Liu-Liang method has the highest percent of cases in which no ABL height is found at all for the DH2 profiles. This trend indicates that, while the Liu-Liang method sometimes works to find an ABL height close to the subjective ABL height, it also fails to find an ABL height close to the subjective ABL height, or to find any ABL height, in many cases. Another important finding is that the Ri_b method using either critical value never fails to find an ABL height and the percent of cases within each percent difference range is greater for the Ri_b method than that for all other methods.

The information presented in the bar graph for the radiosonde profiles (Fig. 10b) leads to a similar conclusion. As for the DH2 profiles, the Ri_b method predicts the highest percent of cases to be within 10% of the subjective ABL height (but for this platform, the critical value of 0.5 does best) and the Liu-Liang method predicts the third highest percent of cases to be within 10% of the subjective ABL height. Additionally, as for the DH2 profiles, the Liu-Liang method performs more poorly as the percent difference range is increased. The Liu-Liang method also has the highest percent of cases in which no ABL height is found at all, followed by the Heffter and TGRDM methods, which was also true for the DH2 data. As for the DH2, there are no radiosonde cases in which the Ri_b method with either critical value finds no ABL height. The main difference between Fig. 10b of the radiosonde data and Fig. 10a of the DH2 data is that, while the Ri_b method with critical value of 0.75 applied to the DH2 data was always more successful than that with critical value of 0.5 for percent difference ranges below 70%, for the radiosonde data, the Ri_b method with critical value of 0.5 proves to always be more successful than that with critical value of 0.75.

Figure 10 goes here

After comparing ABL height from the different objective methods to the subjective ABL height for both the DH2 and the radiosondes (Fig. 9 - 10), it is found that, with the exception of the Liu-Liang method, all other methods generally provide a reasonable estimate of ABL height for both datasets, with the Ri_b method being most favorable. Additionally, the efficacy of each method is similar for the DH2 and the radiosonde data, as is indicated by similar patterns in the scatter plots (Fig. 9) and bar plots (Fig. 10).

3.2 When the objective methods fail

595   While the Liu-Liang method sometimes works well, it is not consistent enough to be reliable across a wide range of different profile structures. Specifically, this method often struggles to accurately predict ABL height of SBLs because the $d\theta_v/dz$ criteria are not met anywhere in the profile, usually because a weak θ_v inversion persists throughout the whole $d\theta_v/dz$ profile, meaning that the method reverts to using the LLJ height as the ABL height. However, the LLJ is usually above the ABL, so this predicts the ABL height to be too high (example: Supplementary Fig. S2 on 24

600   March at 12:09 UTC). If there is no LLJ in the profile and a weak θ_v inversion persists throughout the whole $d\theta_v/dz$ profile, then the Liu-Liang method will not identify any ABL height (example: Supplementary Fig. S29 on 30 April at 14:07 UTC). In most NBL cases, the Liu-Liang method is very successful, but it fails when there is a gradual transition between the ABL and the entrainment zone, as opposed to a sharp change in θ_v slope at the top of the ABL (example: Supplementary Fig. S50 on 17 July at 13:30 UTC).

605

Any of the other objective methods would be a good choice for objectively determining ABL height for a dataset similar to the DH2 and radiosonde datasets (high resolution profiles in the central Arctic environment). However, each method still struggles in some situations, which leads them to either over- or underestimate ABL height. The Heffter method sometimes estimates an ABL height above what is identified as the subjective ABL height when there is a

610   neutral ABL with constant θ_v with altitude, capped by a weak θ_v inversion (minimal θ_v change with altitude). Because the Heffter method identifies the ABL height as the point where θ_v is 2 K warmer than θ_v at the bottom of the θ_v inversion then, in such a scenario this method would identify the ABL as part way through the entrainment zone, while the subjective criteria identify the top of the ABL to be the bottom of the entrainment zone (example: Supplementary Fig. S52 on 18 July 13:10 UTC). The Heffter method also struggles to identify the ABL height of a SBL where the

615   ABL may extend beyond the altitude at which θ_v is 2 K warmer than θ_v at the surface (example: Supplementary Fig. S1 on 23 March at 13:52 UTC) or may not extend all the way to the altitude at which θ_v is 2 K warmer than θ_v at the surface (example: Supplementary Fig. S38 on 21 June at 13:13 UTC).

The TGRDM method sometimes struggles to identify the correct ABL height, since it identifies the strongest point of

620   the θ_v inversion as the ABL height. While this often occurs at the altitude identified as the subjective ABL height, it also sometimes occurs part way through the entrainment zone, resulting in the ABL height estimation by the TGRDM method to be too high (example: Supplementary Fig. S60 on 22 July at 7:37 UTC). This approach also fails in cases of strong surface-based inversions, where the largest θ_v gradient would be at the surface but the ABL would extend some distance above the surface, as a result of mechanically generated turbulence, despite the strong static stability near the surface. While the DH2 dataset did not have any cases in which the surface-based inversion was strongest

625   right at the surface, this problem did arise in some radiosonde profiles (example: Supplementary Fig. S6 on 7 April) due to the elimination of the near-surface datapoints. It is possible that similar situations may arise when analyzing other datasets, especially in the middle of wintertime in the Arctic.

630 Lastly, the Ri_b method may fail if Ri_b is not accurately capturing the transition from turbulent to laminar conditions or if the critical values used are not accurate for certain cases (examples: Supplementary Fig. S4 on 29 March 12:24 UTC and S41 on 30 June 8:39 UTC). Table 3 lists the cases in which the objective ABL height differs by more than 50% from the subjective ABL height for the DH2 data, or no ABL height was found, which can be referenced in the Supplementary Figures for examples of certain profile structures that are not as conducive to the success of the

635 different objective methods. When applying these objective methods to a large dataset to automatically identify ABL height, it is recommended that some level of pre-screening is applied to flag cases that contain certain features or structural patterns that would make certain objective methods have difficulty identifying ABL height, and choosing which objective method to use based on that.

640 **Table 3 goes here**

Overall, the objective methods are more likely to agree with each other as well as with the subjective ABL for cases with more simplistic structures, such as those with strong potential temperature inversions with a base at or just below the top of the ABL, those with LLJ core altitude at or just above the top of the ABL, and those with consistently and

645 somewhat gradually increasing θ_v with altitude above the entrainment zone.

4. Summary and conclusions

By comparing subjective ABL heights identified visually in θ_v, humidity (both RH and mixing ratio), and Ri_b profiles to objectively determined ABL heights, the performance of several different published methods, including the Liu-

650 Liang, Heffter, TGRDM, and Ri_b methods, are evaluated across 65 DH2 profiles. When comparing objective to subjective ABL height for each DH2 case, the method that appears to be most successful (combination of high R^2 value, low p-value, and slope close to 1) is the Ri_b method with either critical value (Fig. 9). When calculating the percent of DH2 cases in which the objective ABL height is within certain percent difference ranges from the subjective ABL height, the Ri_b method with a critical value of either 0.5 or 0.75 is also most successful (Fig. 10). The Heffter

655 and TGRDM methods also produce reasonable results according to Fig. 9 and 10. The only objective method that consistently fails at accurately identifying ABL height is the Liu-Liang method.

In the process of applying these different objective methods to the DH2 data, some threshold and qualifying values were modified to be better applicable to the UAS dataset. While these adjustments were made to best suit the 65 DH2

660 profiles analyzed in this study which occurred between March and July of 2020, these adjustments should yield better results for identifying ABL height during any season and location in the central Arctic. We hypothesize this because the ABL structures sampled by the DH2 in the current study were diverse and encompass the variety of ABL structures commonly observed in the central Arctic (which are typically shallow and either stable or neutral) throughout the entire year. Additionally, since the locations of the DH2 flights in this study range from deep in the sea ice pack to

665 near the sea ice edge, we are confident that the adjustments made will be applicable for identifying ABL height in either environment.

Testing these adjustments outside of the 65 DH2 flights, the modified techniques were also applied to the radiosonde profiles closest in time to each DH2 flight, to determine if the methods work similarly on data from another sensing platform. To test this, the processes of subjective and objective ABL height identification described for the DH2 profiles were repeated on the radiosonde profile closest in time to each DH2 flight. Radiosonde profiles closest in time proximity to the DH2 flights were used under the assumption that the ABL structure would be minimally changed between the launch of the two platforms (supported by Fig. 8), and thus applying the methods of subjective and objective ABL height detection would lead to a similar conclusion. For the radiosonde data, the Heffter and Ri_b methods prove most successful for the radiosondes in terms of having a high R^2 value, low p-value, and slope closest to 1 when compared to the other objective methods (Fig. 9). Additionally, the Ri_b method also proves most successful when looking at the percent of cases in which the objective ABL height was within different percent difference ranges for the radiosondes, as it did for the DH2 (Fig. 10). Once again, the only method that consistently provided unfavorable results is the Liu-Liang method. These similar conclusions demonstrates that the adapted objective methods are indeed robust across platforms.

These findings show that no one method works well 100% of the time. Given this, the best way to accurately identify ABL height across a variety of conditions in the Arctic atmosphere is to visually analyze the θ_v, humidity, and Ri_b profiles for each case individually. However, in the case of large datasets that require automated processing techniques, the current study reveals that the Ri_b, Heffter, or TGRDM methods are most suitable for such a task, with the preferred method being the Ri_b method with critical value of 0.5. The Liu-Liang method does not provide consistent results in accurately identifying Arctic ABL heights in many cases, especially SBLs (Fig. 9 - 10). The most common occurrence of failure of the objective methods exists for NBLs capped by a weak θ_v inversion, so that a clear θ_v slope change between the ABL and entrainment zone is difficult to find. In such cases, the Ri_b method was found to be most reliable for identifying the ABL height.

The methods and results of this study for stability regime and ABL height identification are currently being applied to the entire year of radiosonde data collected during the MOSAiC expedition (October 2019 – September 2020) to create a data product containing year-long statistics on ABL characteristics in the central Arctic. Additional metrics, such as low-level jet height and speed and temperature inversion depth and strength will be included in this product for eventual publication. Additional value from the DH2 data and methods used in the current study comes from the uniqueness of the location and timing of the profiles collected, so these data provide a unique opportunity to evaluate any additional ABL height detection schemes that were not addressed in this study, or that have yet to be developed.

Data availability

All DataHawk2 data used in this study are openly available from the National Science Foundation Arctic Data Center at *insert DOI when available* (Jozef et al., 2021) as described in de Boer et al. (in progress). Due to its proprietary nature, radiosonde data is not yet openly available to the public, aside from official MOSAiC project members. Further

information about the data and conditions for access are available at the PANGAEA Data Publisher at
705   https://doi.org/10/1594/PANGAEA.928656 (Maturilli et al., 2021).

Author contributions

GdB and JC planned the DH2 data collection and acquired funding; GJ and JC conducted DH2 flights; GJ, JC, and
GdB conceptualized the analysis presented in this paper; GJ analyzed the data; GJ wrote the manuscript; JC, SD, and
710   GdB reviewed and edited the manuscript.

Competing interests

The authors declare that they have no conflict of interest.

715   **Acknowledgments**

Data used in this paper were produced as part of *RV Polarstern* cruise AWI_PS122 and of the international
Multidisciplinary drifting Observatory for the Study of the Arctic Climate (MOSAiC) with the tag MOSAiC20192020.
We thank all those who contributed to MOSAiC and made this endeavor possible (Nixdorf et al., 2021). Radiosonde
data were obtained through a partnership between the leading Alfred Wegener Institute (AWI), the Atmospheric
720   Radiation Measurement (ARM) User Facility, a US Department of Energy facility managed by the Biological and
Environmental Research Program, and the German Weather Service (DWD). Non-author contributors to DH2 design,
data collection, and data processing include Dale Lawrence[1], Jonathan Hamilton[1,2,4], Radiance Calmer[2,3], Brian
Argrow[1,5], Steven Borenstein[1,5], Abhiram Doddi[1], Julia Schmale[6], and Andreas Preußer[7].

[1]Dept. of Aerospace Engineering Sciences, University of Colorado Boulder
725   [2]Cooperative Institute for Research in Environmental Sciences, University of Colorado Boulder
[3]National Snow and Ice Data Center, University of Colorado Boulder
[4]NOAA Physical Sciences Laboratory
[5]Integrated Remote and In-Situ Sensing, University of Colorado Boulder
[6]Swiss Federal Institute of Technology Lausanne
730   [7]University of Trier

Financial support

Collection and analysis of atmospheric boundary layer data with the DataHawk2 was funded by the National Science
Foundation (award OPP 1805569, de Boer, PI). Additional funding and support were provided by the Cooperative
735   Institute for Research in Environmental Sciences, the National Oceanic and Atmospheric Administration Physical
Sciences Laboratory, and the Alfred Wegener Institute.

References

Alfred-Wegener-Institut Helmholtz-Zentrum für Polar- und Meeresforschung: Polar
740   Research and Supply Vessel POLARSTERN operated by the Alfred-Wegener-Institute, Journal of Large-
Scale Research Facilities, 3, 1-8, https://doi.org/10.17815/jlsrf-3-163, 2017.

Andreas, E. L., Horst, T. W., Grachev, A. A., Persson, P. O. G., Fairall, C. W., Guest, P. S., and Jordan, R. E.:
Parametrizing turbulent exchange over summer sea ice and the marginal ice zone, Quart. J. Roy. Meteor. Soc.,
136, 927–943, https://doi.org/10.1002/qj.618, 2010.

745 Brooks, I. M., Tjernström, M., Persson, P. O. G., Shupe, M. D., Atkinson, R. A., Canut, G., Birch, C. E., Mauritsen,
T., Sedlar, J., and Brooks, B. J.: The Turbulent Structure of the Arctic Summer Boundary Layer During The
Arctic Summer Cloud-Ocean Study, J. Geophys. Res.: Atmos., 122, 9685–9704,
https://doi.org/10.1002/2017JD027234, 2007.

Dai, C., Gao, Z., Wang, Q., Cheng, G.: Analysis of Atmospheric Boundary Layer Height
750 Characteristics over the Arctic Ocean Using the Aircraft and GPS Soundings, Atmos. Oceanic Sci. Lett., 4,
124-130, https://doi.org/10.1080/16742834.2011.11446916, 2011.

Dai, C., Wang, Q., Kalogiros, J. A., Lenschow, D. H., Gao, Z., and Zhou, M.: Determining
Boundary-Layer Height from Aircraft Measurements, Boundary-Layer Meteorology, 152, 277–302,
https://doi.org/10.1007/s10546-014-9929-z, 2014.

755 Jozef, G., de Boer, G., Cassano, J., Calmer, R., Hamilton J., Lawrence, D., Borenstein, S., Doddi, A., Schmale, J.,
Preußer, A., Argrow, B.: DataHawk2 Uncrewed Aircraft System data from the Multidisciplinary drifting
Observatory for the Study of Arctic Climate (MOSAiC) campaign, B1 level, Arctic Data Center, submitted
2021.

de Boer, G., Chapman, W., Kay, J. E., Medeiros, B., Shupe, M. D., Vavrus, S., and Walsh, J.: A Characterization of
760 the Present-day Arctic Atmosphere in CCSM4, J. Climate, 25, 2676–2695, https://doi.org/10.1175/JCLI-D-11-
00228.1, 2021.

de Boer, G., Calmer, R., Jozef, G., Cassano, J., Hamilton, J., Lawrence, D., Borenstein, S., Doddi, A.,
Cox, C., Schmale, J., Preußer, A. and Argrow, B.: Observing the Central Arctic Atmosphere and Surface
with University of Colorado Uncrewed Aircraft Systems, Nature Sci. Data, in progress 2021.

765 Delle Monache, L., Perry, K. D., Cederwall, R. T., and Ogren, J. A.: In Situ Aerosol Profiles over the Southern
Great Plains Cloud and Radiation Test Bed Site: Effects of Mixing Height on Aerosol Properties, J. Geophys.
Res., 109, 1-9, https://doi.org/10.1029/2003jd004024, 2004.

Esau, I., and Sorokina, S.: Climatology of the Arctic Planetary Boundary Layer, in: Atmospheirc Turbulence,
Meteorological Modeling and Aerodynamics, Nova Science Publishers, Inc, New York, 3-58, 2010.

770 Grachev, A. A., Fairall, C. W., Persson, P. O. G., Andreas, E. L., and Guest, P. S.: Stable Boundary-layer Scaling
Segimes: The SHEBA Data, Boundary-Layer Meteor., 116, 201–235, https://doi.org/10.1007/s10546-004-
2729-0, 2005.

Hamilton, J., de Boer, G., Lawrence, D.: The DataHawk2: An Innovative Small Unmanned Aircraft for Atmospheric
Science Research, in progress 2021.

775 Heffter, J. L., 1980: Transport layer depth calculations, in: Proc. Second Joint Conf. on
Applications of Air Pollution Modelling, New Orleans, LA, Amer. Meteor. Soc., 787–791.

Jenkins, A. D., Paskyabi, M. B., Fer, I., Gupta, A., and Adakudlu, M.: Modelling the effect of ocean waves on the
atmospheric and ocean boundary layers, Energy Procedia, 24, 166–175,

https://doi.org/10.1016/j.egypro.2012.06.098, 2012.

780   Karlsson, J., and Svensson, G.: Consequences of Poor Representation of Arctic Sea-ice Albedo and Cloud-radiation
Interactions in the CMIP5 Model Ensemble, Geophys. Res. Lett., 40, 4374–4379,
https://doi.org/10.1002/grl.50768, 2013.

Liu, S., and Liang, X. Z.: Observed Diurnal Cycle Climatology of Planetary Boundary Layer Height, J. Climate, 23,
5790–5809, https://doi.org/10.1175/2010JCLI3552.1, 2010.

785   Lüpkes, C., Vihma, T., Bimbaum, G., and Wacker, U.: Influence of Leads in Sea Ice on the Temperature of the
Atmospheric Boundary Layer during Polar Night, Geophys. Res. Lett., 35, 2–6,
https://doi.org/10.1029/2007GL032461, 2008.

Marsik, F. J., Fischer, K. W., McDonald, T. D., and Samson, P. J.: Comparison of Methods
for Estimating Mixing Height Used during the 1992 Atlanta Filed Intensive, J. Appl. Meteor., 34, 1802–1814,
790   https://doi.org/10.1175/1520-0426(1999)016<0584:ACOMDO>2.0.CO;2, 1995.

Maturilli, M., Holdridge, D. J., Dahlke, S., Graeser, J., Sommerfeld, A., Jaiser, R., Deckelmann, H.,
and Schulz, A.: Initial radiosonde data from 2019-10 to 2020-09 during project MOSAiC, Alfred Wegener
Institute, Helmholtz Centre for Polar and Marine Research, Bremerhaven, PANGAEA,
https://doi.org/10.1594/PANGAEA.928656, 2012.

795   Mayer, S., Jonassen, M. O., Sandvik, A., and Reuder, J.: Profiling the Arctic Stable Boundary Layer in Advent
Valley, Svalbard: Measurements and Simulations, Boundary-Layer Meteor., 143, 507–526,
https://doi.org/10.1007/s10546-012-9709-6, 2012.

Nicolaus, M., et al.: Overview of the MOSAiC expedition – Snow and Sea Ice, Elementa, submitted.

Nixdorf, U., Dethloff, K., Rex, M., Shupe, M., Sommerfeld, A., Perovich, D., Nicolaus, M.,
800   Heuzé, C., Rabe, B., Loose, B., Damm, E., Gradinger, R., Fong, A., Maslowski, W., Rinke, A., Kwok, R.,
Spreen, G., Wendisch, M., Herber, A., Hirsekorn, M., Mohaupt, V., Frickenhaus, S., Immerz, A., Weiss-
Tuider, K., König, B., Mengedoht, D., Regnery, J., Gerchow, P., Ransby, D., Krumpen, T., Morgenstern, A.,
Haas, C., Kanzow, T., Rack, F. R., Saitzev, V., Sokolov, V., Makarov, A., Schwarze, S., Wunderlich, T.,
Wurr, K., and Boetius, A.: MOSAiC Extended Acknowledgement, Zenodo,
805   https://doi.org/10.5281/zenodo.5179738, 2021.

Pesenson, I.: Implementation and Evaluation of the Heffter Method to Calculate the Height of the Planetary
Boundary Layer above the ARM Southern Great Plains Site, Lawrence Berkeley National Lab.,
https://escholarship.org/uc/item/6pp1d93m, 2003.

Seibert, P., Beyrich, F., Gryning, S. E., Joffre, S., Rasmussen, A., and Tercier, P.: Review and Intercomparison of
810   Operational Methods for the Determination of the Mixing Height, Atmos. Environ., 34, 1001–102,
https://doi.org/10.1016/S1474-8177(02)80023-7, 2000.

Shupe, M. D., Rex, M., Dethloff, K., Damm, E., Fong, A. A., Gradinger, R., Heuzé, Loose, C., B., Makarov, A.,
Maslowski, W., Nicolaus, M., Perovich, D., Rabe, B., Rinke, A., Sokolov, V., and Sommerfeld, A.: The
MOSAiC Expedition : A Year Drifting with the Arctic, NOAA Arctic Report Card, 1–8,
815   https://doi.org/10.25923/9g3v-xh92, 2020.

Shupe, M. D., et al.: Overview of the MOSAiC Expedition – Atmosphere, Elementa, submitted.

Sivaraman, C., Mcfarlane, S., Chapman, E., Jensen, M., Toto, T., Liu, S., and Fischer, M.: Planetary Boundary
    Layer (PBL) Height Value Added Product (VAP) : Radiosonde Retrievals. Atmos. Radiat. Meas., 2013.

Snyder, B. J., and Strawbridge, K. B.: Meteorological Analysis of the Pacific 2001 Air Quality Field Study, Atmos.
820   Environ., 38, 5733–5743, https://doi.org/10.1016/j.atmosenv.2004.02.068, 2004.

Steeneveld, G. J., van de Wiel, B. J. H., and Holtslag, A. A. M.: Diagnostic equations for the stable boundary layer
    height: Evaluation and dimensional analysis, J. Appl. Meteor. Climatol., 46, 212–225,
    https://doi.org/10.1175/JAM2454.1, 2007.

Stroeve, J., Holland, M. M., Meier, W., Scambos, T., and Serreze, M.: Arctic Sea Ice Decline: Faster than Forecast,
825   Geophys. Res. Lett., 34, 1–5, https://doi.org/10.1029/2007GL029703, 2007.

Stroeve, J. C., Kattsov, V., Barrett, A., Serreze, M., Pavlova, T., Holland, M., and Meier, W. N.: Trends in Arctic
    Sea Ice Extent from CMIP5, CMIP3 and Observations, Geophys. Res. Lett., 39, 1–7,
    https://doi.org/10.1029/2012GL052676, 2012.

Stull, R. B.: An Introduction to Boundary Layer Meteorology. Kluwer Academic Publishers, 1988.

830 Tjernström, M., Leck, C., Persson, P. O. G., Jensen, M. L., Oncley, S. P., and Targino, A.: The Summertime Arctic
    Atmosphere: Meteorological Measurements during the Arctic Ocean Experiment 2001, Bull. Amer. Meteor.
    Soc., 85, 1305–1321, https://doi.org/10.1175/BAMS-85-9-1305, 2004.

Tjernström, M., Birch, C. E., Brooks, I. M., Shupe, M. D., Persson, P. O. G., Sedlar, J., Mauritsen, T., Leck, C.,
    Paatero, J., Szczodrak, M., and Wheeler, C. R.: Meteorological Conditions in the Central Arctic Summer
835   during the Arctic Summer Cloud Ocean Study (ASCOS), Atmos. Chem. Phys., 12, 6863–6889,
    https://doi.org/10.5194/acp-12-6863-2012, 2012.

Zhang, Y., Gao, Z., Li, D., Li, Y., Zhang, N., Zhao, X., and Chen, J.: On the Computation of Planetary Poundary-
    Layer Height using the bulk Richardson Number Metho, Geosci. Model Dev., 7, 2599–2611,
    https://doi.org/10.5194/gmd-7-2599-2014, 2014.

840 Zilitinkevich, S., and Baklanov, A.: Calculation of the Height of the Stable Boundary Layer in Practical
    Applications, Boundary-Layer Meteor., 105, 389–409, https://doi.org/10.1023/A:1020376832738, 2002.

Tables

845

Table 1: List of variables previously used to identify ABL height, as well as the associated literature in which each variable was referenced.

Variable	Previous Literature
virtual potential temperature	Heffter, 1980; Stull, 1988; Seibert et al., 2000; Pesenson, 2003; Dai et al., 2011; Sivaraman et al., 2013; Dai et al., 2014; Zhang et al., 2014
vertical gradient of virtual potential temperature	Heffter, 1980; Stull, 1988; Liu and Liang, 2010; Dai et al., 2011; Sivaraman et al., 2013; Dai et al., 2014
vertical gradient of temperature	Stull, 1988
bulk Richardson number	Stull, 1988; Seibert et al., 2000; Zilitinkevich and Baklanov, 2002; Steeneveld et al., 2007; Dai et al., 2011; Sivaraman et al., 2013; Dai et al., 2014; Zhang et al., 2014
total wind speed	Stull, 1988; Seibert et al., 2000; Liu and Liang, 2010; Steeneveld et al., 2007; Sivaraman et al., 2013; Zhang et al., 2014
component-wise wind speed perturbations	Dai et al., 2011; Dai et al., 2014; Zhang et al., 2014
wind shear	Dai et al., 2014
liquid water content and absolute humidity	Seibert et al., 2000; Pesenson, 2003; Dai et al., 2014
turbulent kinetic energy	Stull, 1988

850 **Table 2:** Accuracy and reliability of the variables recorded by the Vaisala RSS-421 sensors used in this study.

Variable	Resolution	Repeatability	Response Time
Pressure	0.01 hPa	0.4 hPa	-
Temperature	0.01 °C	0.1 °C	0.5s
Humidity	0.1 %RH	2 %RH	<0.3s (at 20 °C) to <10s (at -40 °C)

Table 3: The Supplementary Figures associated with cases in which the objective ABL height was greater than 50% different than the subjective ABL height, or no objective ABL height was found.

855

Objective Method			
Liu-Liang	**Heffter**	**TGRDM**	**Ri_{bc} = 0.5 or 0.75**
S2, S5, S6, S7, S9, S10, S13, S14, S15, S20, S25, S26, S27, S28, S29, S30, S31, S34, S37, S42, S44, S45, S48, S50, S51, S53, S54, S55, S56, S58, S60, S61, S62, S64	S1, S11, S12, S13, S21, S25, S28, S29, S30, S36, S37, S41, S43, S44, S47, S48, S50, S51, S52, S54, S55, S62	S8, S9, S10, S20, S21, S25, S28, S41, S42, S48, S50, S53, S54, S55, S56, S60, S62	S4, S13, S48, S53, S62

Figures
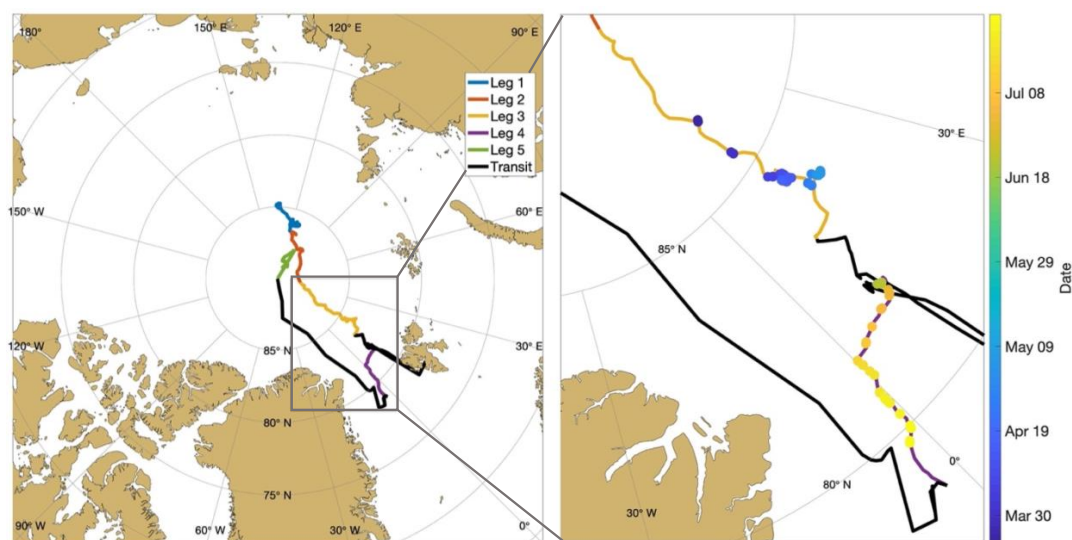
860

Figure 1: (Left) The drift track of the *Polarstern*, separated by color into the 5 different legs. The black "transit" line indicates when the ship was travelling under its own power between legs 3 and 4 and between legs 4 and 5. **(Right)** The zoomed in portion of the *Polarstern* drift during which DH2 flights were conducted (legs 3 and 4). The locations of all of the DH2 flights are overlaid on the drift track and color coded by date, with blue-tinted dots indicating flights conducted during leg 3 and yellow-tinted dots indicating flights conducted during leg 4.

865
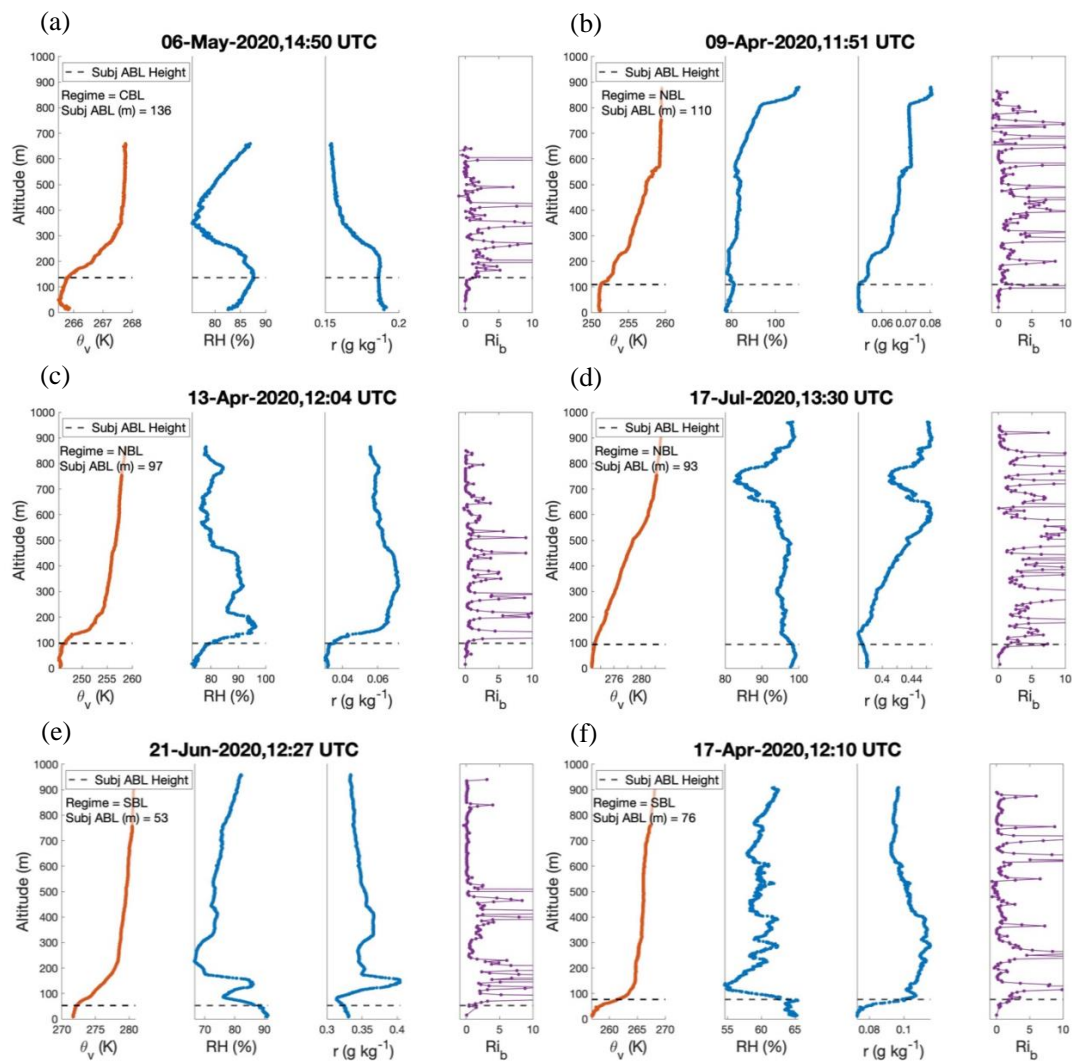
Figure 2: For each flight, the θ$_v$ profile (orange) is plotted in the left panel, the RH and mixing ratio profiles (blue) are plotted in the middle two panels, and the Ri$_b$ profile (purple) is plotted on the right panel. The subjective ABL height is marked with a dotted black line on each panel, and is written, along with stability regime, on the left panel. **(a)** Example of a CBL case. **(b – d)** Examples of NBL cases. **(e – f)** Examples of SBL cases.
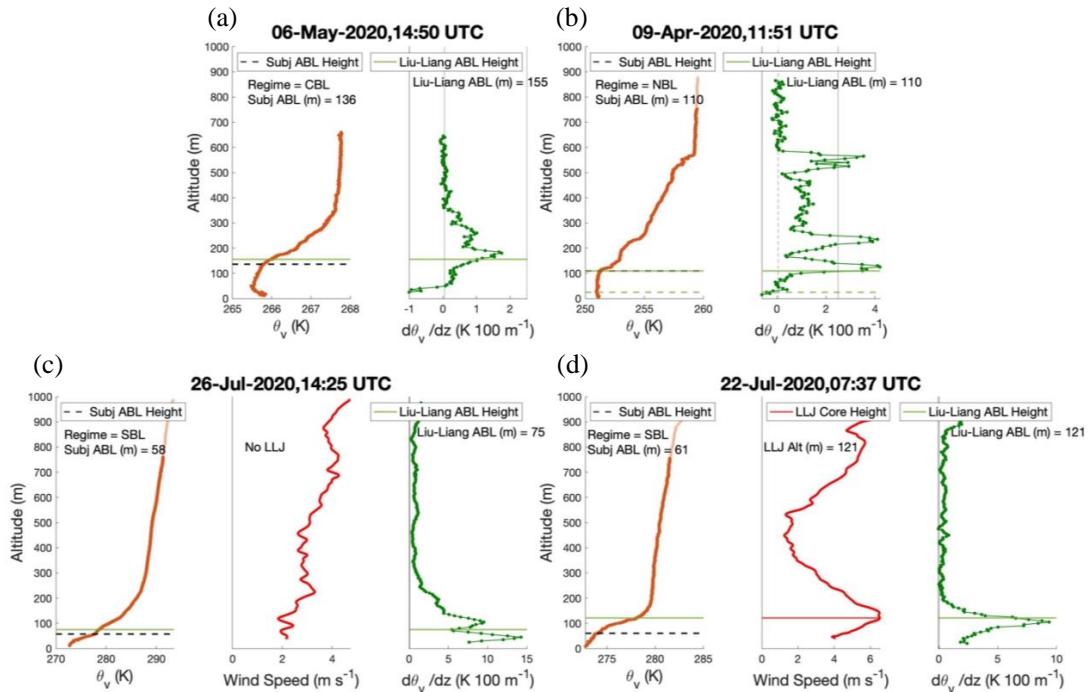
Figure 3: Examples of ABL height identification using the Liu-Liang method for the different stability regimes. For each of the above cases, the θ_v profile is plotted in the left panel, and the subjective ABL height is marked with a dotted black line. The ABL regime as well as the subjective ABL height are written below the legend on the θ_v plot. The right panel in each case shows the $d\theta_v/dz$ profile, and the ABL height identified by the Liu-Liang method is marked with a green line and the altitude written below the legend. This green line is also included on the θ_v profile. For the two SBL cases (bottom), a middle panel showing the wind speed profile is included, indicating the location and altitude of the LLJ, if one is present. **(a)** For the CBL case, a thin black line at $d\theta_v/dz = 0.05$ K/100 m is plotted on the right panel. **(b)** For the NBL case, a thin black line at $d\theta_v/dz = 2.5$ K/100 m is plotted on the right panel. Additionally, a dashed black line using the original Liu-Liang threshold value of $d\theta_v/dz = 0.05$ K/100 m is plotted on the right panel, as well as a dashed green line at the ABL height associated with using this threshold on both panels. **(c)** For a SBL case, the ABL found by the Liu-Liang methods is determined using the first buoyancy forcing criteria. **(d)** For another SBL case, the ABL found by the Liu-Liang methods is determined as the altitude of the LLJ. For both SBL cases, a thin black line at $d\theta_v/dz = 0.05$ K/100 m is plotted on the right panel.
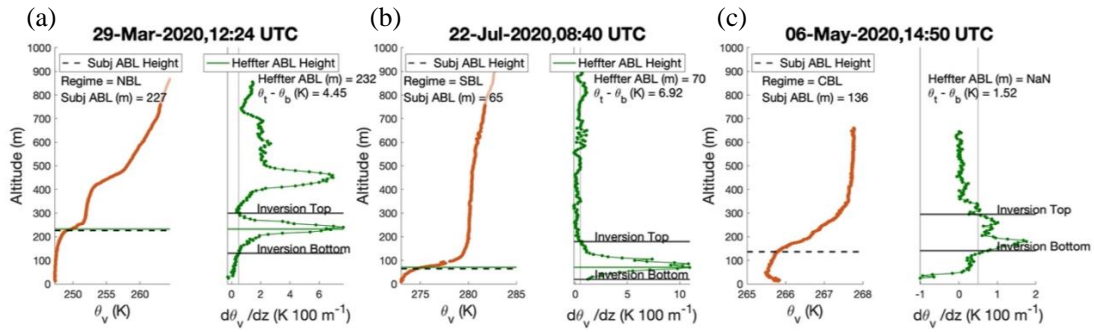
Figure 4: Examples of ABL height identification using the Heffter method applied to **(a)** a NBL case, **(b)** a SBL case, and **(c)** a CBL case. For each of the above cases, the θ_v profile is plotted in the left panel, and the subjective ABL height is marked with a dotted black line. The ABL regime as well as the subjective ABL height are written below the legend on the θ_v plot. The right panel in each case shows the $d\theta_v/dz$ profile, and the ABL height identified by the Heffter method is marked with a green line and the altitude written below the legend. The green line at the Heffter ABL height is also included on the θ_v profile. Additionally, the θ_v difference across the θ_v inversion is written. A thin black line is plotted at $d\theta_v/dz = 0.5$ K/100 m, and the top and bottom of the θ_v inversion are labeled.
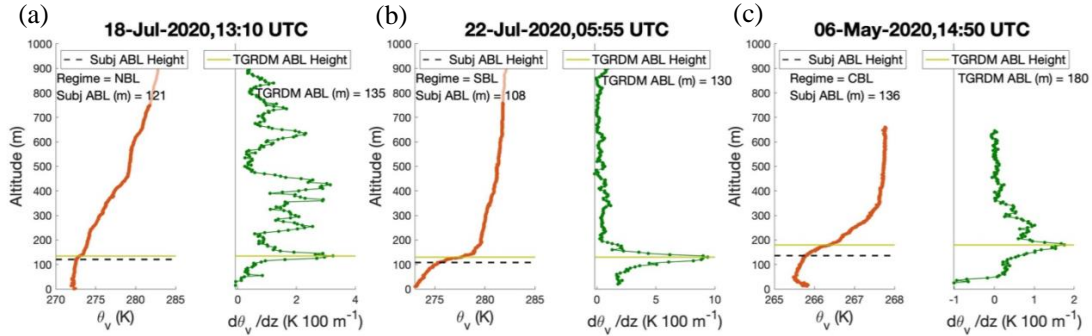
Figure 5: Examples of ABL height identification using the TGRDM method applied to **(a)** a NBL case, **(b)** a SBL case, and **(c)** a CBL case. For each of the above cases, the θ_v profile is plotted in the left panel, and the subjective ABL height is marked with a dotted black line. The ABL regime as well as the subjective ABL height are written below the legend on the θ_v plot. The right panel in each case shows the $d\theta_v/dz$ profile, and the ABL height identified by the TGRDM method is marked with a green line and the altitude written below the legend. This green line at the TGRDM ABL height is also included on the θ_v plot.
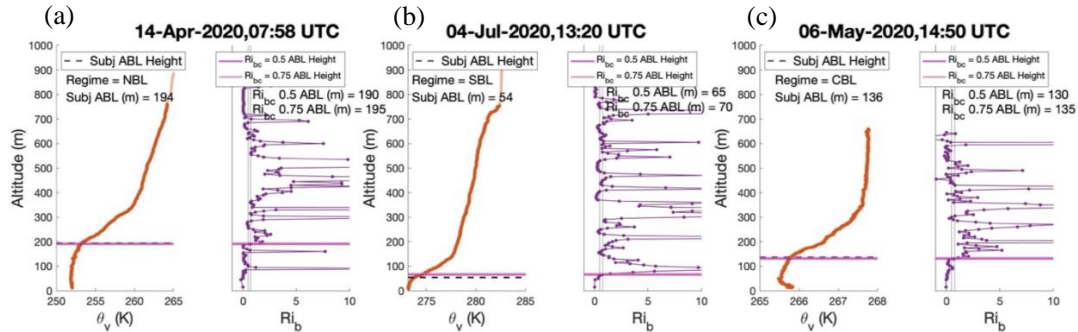
Figure 6: Examples of ABL height identification using the Ri_b method applied to **(a)** a NBL case, **(b)** a SBL case, and **(c)** a CBL case. For each of the above cases, the θ_v profile is plotted in the left panel, and the subjective ABL height is marked with a dotted black line. The ABL regime as well as the subjective ABL height are written below the legend on the θ_v plot. The right panel in each case shows the Ri_b profile with vertical black lines plotted at $Ri_b = 0.5$ and $Ri_b = 0.75$. The ABL heights identified by each Ri_{bc} value are marked with pink lines, and the altitude of the ABL height identified by each Ri_{bc} value are written on the right panel. The pink Ri_b ABL height lines are also included on the θ_v plot.
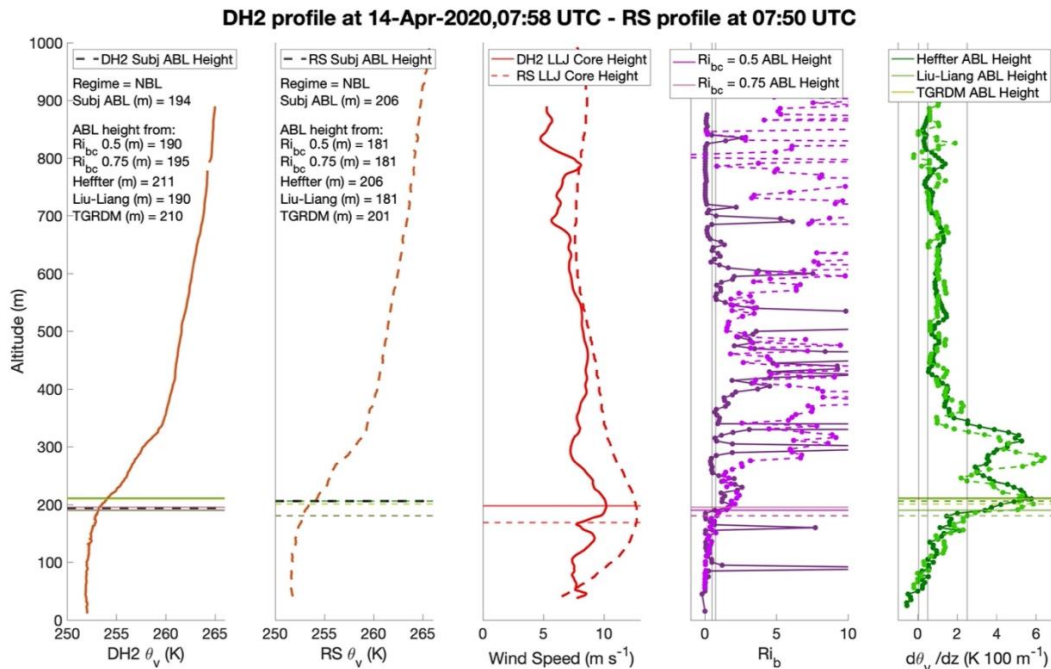
Figure 7: Example of ABL height identification for DH2 flight on 14 April at 7:58 UTC and radiosonde profile at 7:50 UTC. For all panels, the legends refer to the horizontal lines in that panel. **(Panel 1)** θ_v profile from the DH2. The stability regime is written and the subjective ABL height is written and marked with a dashed black line. The ABL height identified by each objective method is written and marked with a solid line of color associated with the legends in the last two panels. **(Panel 2)** θ_v profile from the radiosonde. The subjective ABL height is marked with a dashed black line. The ABL height identified by each objective method is written and marked with a dashed line of

color associated with the legends in the last two panels. **(Panel 3)** wind speed profiles from the DH2 (solid) and radiosonde (dashed) with the location of the low-level jet identified in the DH2 profile marked with a solid horizontal line, and the location of the low-level jet identified in the radiosonde profile marked with a dashed horizontal line. **(Panel 4)** Ri_b profiles from the DH2 (solid dark purple) and the radiosonde (dashed light purple). The ABL heights identified by the Ri_b method using critical values of 0.5 and 0.75 are marked with solid horizontal lines for the DH2 profile and dashed horizontal lines for the radiosonde profile. **(Panel 5)** $d\theta_v/dz$ profiles from the DH2 (solid dark green) and the radiosonde (dashed light green). The ABL heights identified by the Heffter, Liu-Liang, and TGRDM methods are marked with solid horizontal lines for the DH2 profile and dashed horizontal lines for the radiosonde profile.
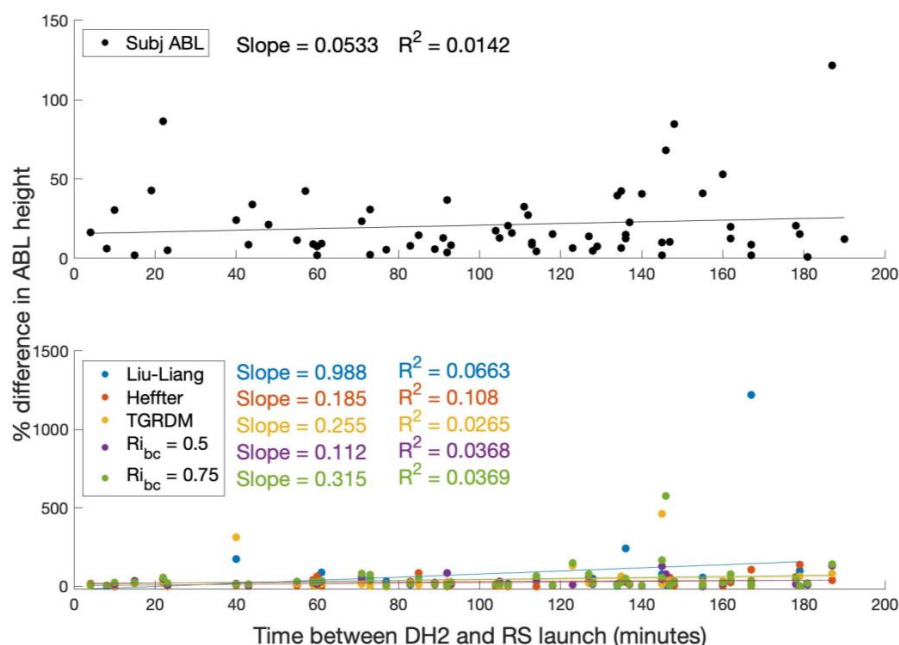
Figure 8: Absolute value of the percent difference between subjective ABL height from the DH2 and subjective ABL height from the radiosonde closest in time to the DH2 launch (black dots, top panel) and absolute value of the percent difference between objective ABL heights from the DH2 and objective ABL heights from the radiosonde closest in time to the DH2 launch (colored dots, bottom panel) versus absolute value of time difference in minutes between the DH2 and radiosonde launches. Lines of best fit are included for the subjective ABL height and for each objective method, and the slope and R^2 values of each line is written next to the legend.
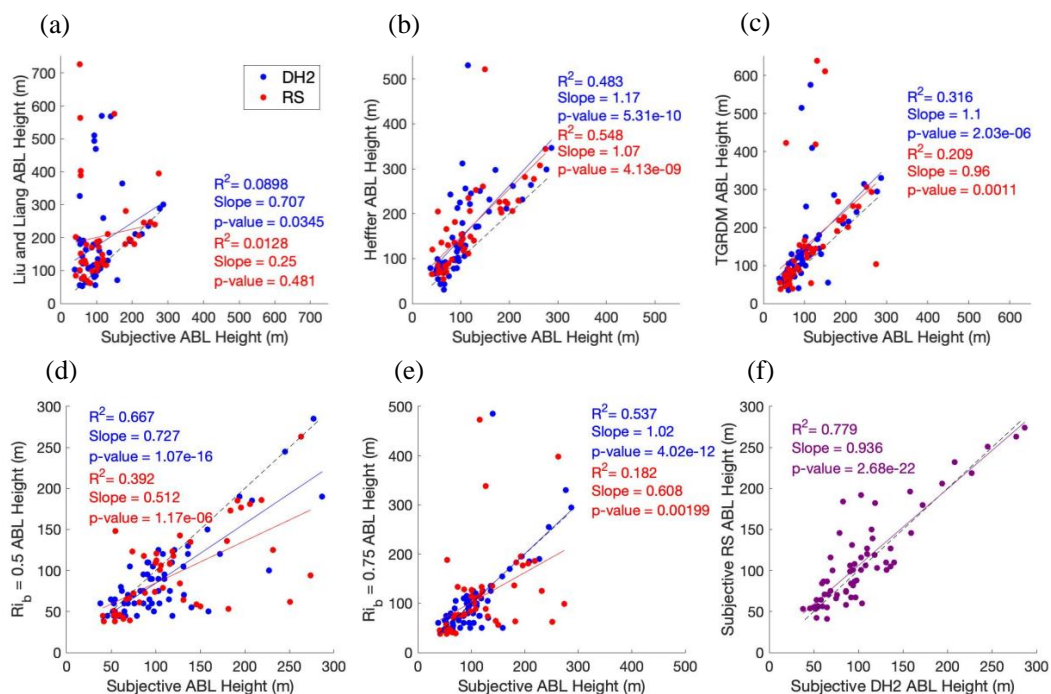
Figure 9: Relationships between subjective ABL height and objective ABL height from the **(a)** Liu-Liang method, **(b)** Heffter method, **(c)** TGDRM method, and **(d,e)** Ri_b method. Blue dots represent DH2 data and red dots represent radiosonde data. The solid blue line (solid red line) on each panel is the line of best fit for the DH2 (radiosonde) data. **(f)** Relationship between subjective ABL height from the radiosonde and subjective ABL height from the DH2 with line of best fit in purple. Each panel is overlaid by the corresponding R^2, slope value, and p-value. The dashed black line on each panel is a line with slope of 1 and y-intercept of 0, for reference.

955

960
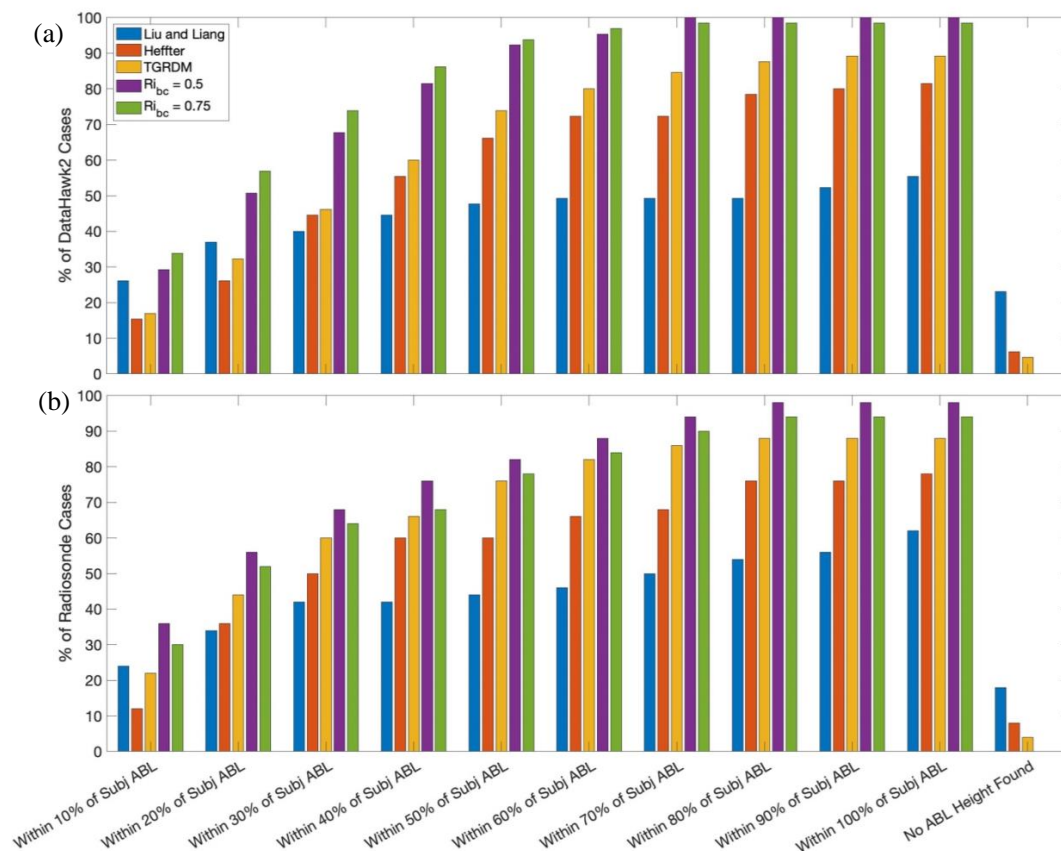
Figure 10: Bar plot showing what percent of **(a)** DH2 cases and **(b)** radiosonde cases give an objective ABL height within different percent difference ranges from the subjective ABL height using the different objective methods. Plot also shows the percent of cases for each method where no ABL height is found.

965